

# PCCP

Accepted Manuscript



This is an *Accepted Manuscript*, which has been through the Royal Society of Chemistry peer review process and has been accepted for publication.

*Accepted Manuscripts* are published online shortly after acceptance, before technical editing, formatting and proof reading. Using this free service, authors can make their results available to the community, in citable form, before we publish the edited article. We will replace this *Accepted Manuscript* with the edited and formatted *Advance Article* as soon as it is available.

You can find more information about *Accepted Manuscripts* in the [Information for Authors](#).

Please note that technical editing may introduce minor changes to the text and/or graphics, which may alter content. The journal's standard [Terms & Conditions](#) and the [Ethical guidelines](#) still apply. In no event shall the Royal Society of Chemistry be held responsible for any errors or omissions in this *Accepted Manuscript* or any consequences arising from the use of any information it contains.

# Transition Metal-doped BiFeO<sub>3</sub> Nanofibers: Forecasting the Conductivity Limit

Qiang Xu,<sup>a</sup> Mushtaq Sobhan,<sup>a</sup> Franklin Anariba,<sup>a</sup> Jeffrey Weng Chye Ho,<sup>b</sup> Zhong Chen,<sup>b</sup>  
and Ping Wu\*<sup>a</sup>

<sup>a</sup>Entropic Interface Group (EIG), Engineering Product Development, Singapore University of Technology and Design (SUTD), 20 Dover drive, Singapore 138682.

<sup>b</sup>School of Materials Science & Engineering, Nanyang Technological University (NTU), 50 Nanyang Avenue, Singapore 639798.

## Abstract

We investigate the limiting electrical conductivity of BiFeO<sub>3</sub> (BFO) nanofibers via first-principles modelling and experiments. Based on a semi-empirical approach, all transition metals are first screened for their suitability to form an acceptor in BFO. The resultant candidates (e.g., Ni, Cu and Ag) are, further studied by more sophisticated electronic structure theory and experiments. Accordingly, a systematic approach in forecasting the electrical conduction in BFO nanofibers is established. The calculated results show that Ag<sup>+</sup> cations prefer substitutions of Bi<sup>3+</sup> while Ni<sup>2+</sup> and Cu<sup>2+</sup> prefer substitution of Fe<sup>3+</sup> sites to form acceptors. All three metals contribute to an increased overall hole concentration which may lead to a conductivity limit in BFO. These predictions were confirmed consistently through the synthesis and electrical testing of Ni-, Cu- and Ag-doped BFO nanofibers. Finally, our results indicate the conductivity limit is approached by Ni doping in BFO. The methodology presented here may be extended to search for the doping conductivity limits of other semiconductors of interest.

## Introduction

BiFeO<sub>3</sub> (BFO) is an important single-phase multiferroic material due to its distinctive ferroelectric, magnetic, piezoelectric, and optical properties including a high Currie temperature of ferroelectricity (T~1100 K) and high Néel temperature of G type antiferromagnetism (T ~650 K).<sup>1-6</sup> The ground state of BFO has a rhombohedral symmetry (space group: R3c), which has large remnant polarization of ~ 90 μCcm<sup>-2</sup>.<sup>7</sup> However, its high leakage current limits the high-dielectric technological applications,<sup>8,9</sup> because of the break down when a large leakage current passes through before the polarization of the device is switched. Hence, concerted efforts have been made on reducing the high leakage current of BFO by using various dopants, for instance, group-II atoms, transition-metal atoms, and rare-earth atoms.<sup>10-16</sup> This “disadvantage” caused by the high leakage current of BFO limits its use

in spintronic and memory applications, however, it can be turned into an “advantage” when used as ionic and electronic conductive materials for photocatalyst applications, and chemical gas sensors. Our recent work show that the Bi vacancies dominate the conductivity of BFO under normal chemical laboratory conditions, that is, oxygen-rich conditions.<sup>17</sup> Every Bi vacancy generates three acceptor defect levels in BFO band gap because of its valence state of +3. Thus, BFO is a p-type semiconductor with a high concentration of holes induced by Bi vacancies. As a consequence, the conductivity of BFO can be tuned by controlling the concentration of Bi vacancies through appropriate doping. Nonetheless, a lack of theoretical guidance on the rationale behind the limiting conductivity, for not only doped BFO, but also a wide range of semiconductors, has bottlenecked the development in photo-catalytic technology.<sup>18-21</sup>

In this work, we report on a theoretical study using first-principles density functional theory (DFT), and supported by experiments, on how to best increase the conductivity through transition metals doping. There are two substituted-cation sites in a BFO cell,  $\text{Fe}^{3+}$  site and  $\text{Bi}^{3+}$  site, and the size relationship for cations and anions is critical for the stability of the structure associated with general perovskites.<sup>22-24</sup> The univalent or divalent ions of dopants are expected to form acceptors defects, enhancing overall BFO conductivity. In order to choose the appropriate dopants, we screened the periodic table of elements according to their ionic radius and their Gibbs free energy of ionization. The screening method used here has already been discussed in ref. 25, for further details also see ref. 26. We find that the low-valent ionic sizes of transition metal atoms are close to  $\text{Fe}^{3+}$ , which means they can occupy  $\text{Fe}^{3+}$  sites with lower strain energies.

The radii of the pertinent transition metal ions, which were selected on the basis of their ionic radius (closer to  $\text{Bi}^{3+}$  and  $\text{Fe}^{3+}$ ) and charge (lower than  $\text{Bi}^{3+}$  and  $\text{Fe}^{3+}$ ) are listed in Table 1. The cations  $\text{Ti}^{2+}$  and  $\text{V}^{2+}$  are ruled out because these ions will introduce higher strain energies due to their much larger radii in comparison to  $\text{Fe}^{3+}$ . Although the sizes of the remaining cations listed in Table 1 are close to  $\text{Fe}^{3+}$ , other factors must be first considered for suitability. Doping with Sc and Co does not enhance the conductivity because there is no increase in the hole concentration, mainly due to their stable 3+ valence state. In the case of Cr, Mn, Ni, and Cu atoms,  $\text{Ni}^{2+}$  and  $\text{Cu}^{2+}$  ions can be formed with lower Gibbs free energy of ionization. As a result, Ni and Cu are chosen as suitable candidates of  $\text{Fe}^{3+}$  site substitution. As for the  $\text{Bi}^{3+}$  site substitution, from all transition metals only  $\text{Ag}^+$  is close in size to  $\text{Bi}^{3+}$ . As a result,  $\text{Ni}^{2+}$ ,  $\text{Cu}^{2+}$ , and  $\text{Ag}^+$  are selected for further analysis. Based on recent works<sup>28</sup>, the dopants of Ni and Cu generate a higher current, whereas Cr and Mn decrease the BFO

conductivity, however, the origin of the high current is still unclear. Furthermore, these theoretical predictions are confirmed experimentally by measuring the electrical properties of Ni-, Cu- and Ag-doped BFO nanofibers.

Table 1. The radii of transition metal ions.<sup>27</sup> The unit of radius is given as Å.

| <i>q</i> | +1   | +2   | +3   |
|----------|------|------|------|
| Bi       | -    | -    | 1.17 |
| Fe       | -    | -    | 0.69 |
| Sc       | -    | -    | 0.89 |
| Ti       | -    | 1.00 | -    |
| V        | -    | 0.93 | -    |
| Cr       | -    | 0.87 | -    |
| Mn       | -    | 0.81 | -    |
| Co       | -    | 0.79 | -    |
| Ni       | -    | 0.83 | -    |
| Cu       | -    | 0.87 | -    |
| Ag       | 1.29 | -    | -    |

### Computational Details

We use the all-electron-like projector augmented wave (PAW) method<sup>29</sup> and the Perdew-Burke-Ernserh of (PBE) exchange correlation potential<sup>30</sup> as implemented in the Vienna Ab-initio Simulation Package (VASP).<sup>31</sup> In this basis, the semicores of Bi, Fe, Ni, Cu, and Ag atoms are treated as valence electrons, for example, 15 valence electrons for Bi ( $5d^{10} 6s^2 6p^3$ ) atom, 16 valence electrons for Fe ( $3s^2 3p^6 3d^6 4s^2$ ) atom, 16 valence electrons for Ni ( $3p^6 3d^9 4s^1$ ), 17 valence electrons for Cu ( $3p^6 3d^{10} 4s^1$ ), and 17 valence electrons for Ag ( $4p^6 4d^{10} 5s^1$ ). In all calculations, the cut-off energy for the plane wave expansion of the wave functions is 500 eV, and the Hellman-Feynman forces are less than 0.01 eV. In the lattice parameters optimization of BFO, the  $9 \times 9 \times 9$  Monkhorst-Pack grid of *k*-points<sup>32</sup> for Brillouin zone integration was used. In the doping calculations, we constructed a 120-atom supercell using its hexagonal conventional cell, in which one of the Bi or Fe atom is replaced with one impurity atom (Ni, Cu, or Ag), corresponding to a doping concentration of 4.17 %. The  $3 \times 3 \times 3$  Monkhorst-pack grid is taken for Brillouin zone in doping calculations. The G-type antiferromagnetic order of the BFO cell with a homogeneous and collinear spin arrangement is maintained in all calculations.<sup>7</sup> In order to analyse the electronic structures of

Ni, Cu and Ag-doped BFO, we employed the PBE+U method to take into account the strong electron correlations of Fe-3d, Ni-3d, and Cu-3d electrons. Here we use the approach described by Dudarev *et al.*,<sup>33</sup> whereby only an effective Hubbard parameter  $U_{eff} = U - J$  enters the Hamiltonian. For the Fe atoms in BFO, its  $U_{eff}$  is taken as 5 eV, which can give closer values to experimental results.<sup>34, 35</sup> The  $U_{eff}$  of Ni, Cu and Ag are of 5.3 eV, 6.52 eV and 5.8 eV, respectively, whose value are taken from their oxides.<sup>36-38</sup>

To determine the defect formation energies and defect transition energy levels, we calculated the total energy  $E(\alpha, q)$  for the system containing the relaxed defect  $\alpha$  ( $\alpha = \text{Ni, Cu, and Ag}$ ) in charge state  $q$ , and the total energy  $E(\text{BFO})$  for the same supercell in the absence of the defect. We also calculated the total energies of all elemental solids or gases at their stable phases. From these quantities, the defect formation energy  $\Delta H_f(\alpha_\beta, q)$  is defined<sup>39</sup> as

$$\Delta H_f(\alpha_\beta, q) = \Delta E(\alpha_\beta, q) + n_\beta \mu_\beta + n_\alpha \mu_\alpha + q E_f. \quad (1)$$

$$\Delta E(\alpha_\beta, q) = E(\alpha_\beta, q) - E(\text{BFO}) + n_\beta \mu_\beta^0 + n_\alpha \mu_\alpha^0 + q E_V. \quad (2)$$

Here,  $\beta$  is Bi or Fe atom,  $E_f$  is Fermi energy of the electrons referenced to valence band maximum (VBM) of BFO ( $E_V$ ).  $\mu_i$  is the chemical potential of constituent  $i$  referenced to elemental solid or gas with chemical potential  $\mu_i^0$ . The  $n$ 's are the number of  $\beta$ , extrinsic defect  $\alpha$ , and the number of electrons  $q$ , transferred from the host to the reservoirs in forming the defect BFO.<sup>40</sup> The defect transition energy level  $\varepsilon_\alpha(q/q')$  is the Fermi energy ( $E_f$ ) in Eq.(1) at which the formation energy  $\Delta H_f(\alpha_\beta, q)$  of defect  $\alpha_\beta$  in charge state  $q$  is equal to that of another charge state  $q'$  of the same defect.<sup>40</sup> That is,

$$\varepsilon_\alpha(q/q') = \frac{\Delta E(\alpha_\beta, q) - \Delta E(\alpha_\beta, q')}{q' - q}. \quad (3)$$

### Experimental Details

First the nanofibers of pristine, Ni-doped, Ag-doped and Cu-doped BFO were synthesized by sol-gel electrospinning method. The precursor solution was prepared by dissolving appropriate hydrous portions of bismuth nitrate  $\text{Bi}(\text{NO}_3)_3 \cdot 5\text{H}_2\text{O}$  and  $\text{Fe}(\text{NO}_3)_3 \cdot 9\text{H}_2\text{O}$  in 2-methoxyethanol to form a 0.8 M solution. A mixture of acetone, DMF and PVP (0.06 gm/ml) were added to the above solution to form a homogeneous 0.2M precursor solution. The volume ratio of acetone to DMF was kept to 1:2. For doping Ni, Ag

and Cu, Ni(CH<sub>3</sub>COO)<sub>2</sub>, AgCl, and CuCl<sub>2</sub> were added separately in the 0.8 M solution before making the 0.2M solution. The concentrations of the dopants were kept at 3wt%. The mixed solution was loaded into a plastic syringe, equipped with a 21 gauge stainless steel needle. The distance between the tip of the syringe needle and the collector of an Al plate was fixed at 13 cm. A positive voltage of 20 kV was applied to the needle while the Al metal collector was grounded. The feeding rate of the solution was adjusted at a constant rate of 0.6 ml h<sup>-1</sup> by using a syringe pump. As-spun nanofibers were collected onto glass substrates (1cm ×1cm) placed onto the metal collector, then dried at 60 °C for 4h, followed by calcination at 550 °C for 2h in air in an oven with a heating rate of 5° C min<sup>-1</sup>.

The microstructure of the synthesized nanofibers was examined using field emission Scanning electron microscopy (FE-SEM, JEOL JSM-7600F) operated at 15 KV accelerating voltage. The crystal structure and phase composition of the annealed nanofibers in powder state was checked by X-ray diffraction (XRD) (Shimadzu XRD-6000, Cu-K $\alpha$  radiation, ( $\lambda$  =1.54 Å). Electrical measurements were conducted using a probe station (Signatone) that was connected to a source meter (6430, Keithly) to perform the measurement. Au electrodes were prepared by depositing 200 nm onto the nanofibers using a shadow mask in a vacuum sputter coating unit.

## Results and Discussion

Fig. 1(a) and 1(b) show the side-view and top-view of the supercell of hexagonal BFO with G-type AFM order. The green and yellow distorted octahedra show the opposite magnetic moment direction of Fe atoms. The optimized structural parameters of Rhombohedral BFO with R3c symmetry obtained using spin-polarized PBE (SPBE) and SPBE+U are reported in Table 2. In general, all sets of optimized parameters are in close agreement with the experimental values. In particular, the lattice constant is overestimated by only 0.7% compared with Kubel and Schmid's results<sup>41</sup>, and the magnetic moment of Fe atom is only 3.4% larger than experimental value.<sup>42</sup> However, the energy gap obtained by using SPBE is 1.04 eV, smaller than experimental value of 2.5 eV.<sup>43</sup> Within the SPBE+U approach, however, its band gap is 2.44 eV, which is in agreement with experimental results. The projected density of states (pDOS) of BFO calculated within SPBE+U approximation is shown in Fig. 1(c). The valence band maximum (VBM) is dominated by O<sub>2p</sub> state. The main O<sub>2p</sub> valence band is found between 0 and -5.5 eV. The main Fe<sub>3d</sub> valence band is focus in a narrow range near -6.5 eV lightly mixed with O<sub>2p</sub> bonding state. The peak of the majority of

$\text{Bi}_{6s}$  state is found between -9 eV and -10 eV. Because the coupling between  $\text{Bi}_{6s}$  and  $\text{O}_{2p}$  state, the antibonding  $\text{Bi}_{6s}$  state is found at the top of valence band.<sup>44</sup> The conduction band minimum (CBM) is mainly dominated by  $\text{Fe}_{3d}$  state, but  $\text{O}_{2p}$  and  $\text{Bi}_{6p}$  states also contribute.

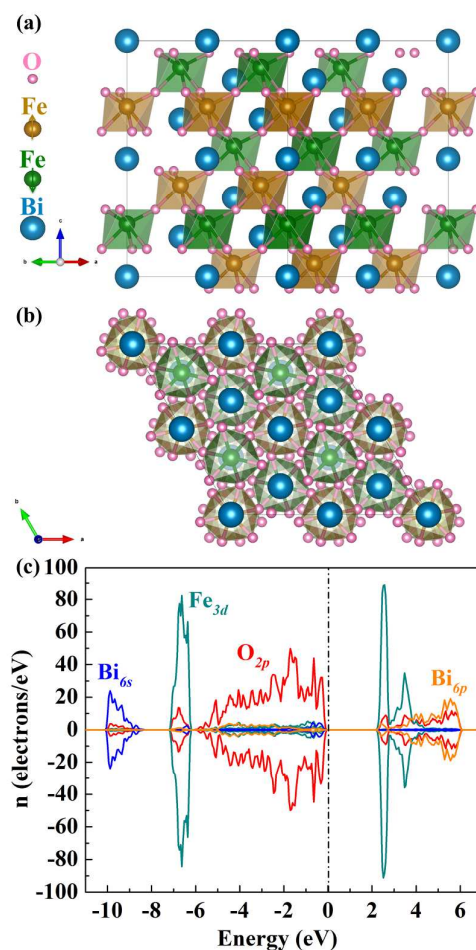


Fig. 1 (Color Online) Representation of the supercell of hexagonal BFO with G-type antiferromagnetic (AFM) order. The green and yellow distorted octahedra show the opposite magnetic moment direction of Fe atoms. (a) side-view of the supercell of hexagonal BFO, (b) top-view of the supercell of hexagonal BFO, and (c) the projected density of states (pDOS) of BFO calculated within spin-polarized PBE+U (SPBE+U) approximation. The dash-dot vertical line is at the fermi level of BFO referenced to valence band maximum (VBM).

Table 2. The equilibrium structural parameters of rhombohedral BFO with R3c symmetry derived from experiments and calculations. The  $E_g$  is the energy band gap, while the  $\mu_{\text{Fe}}$  is the magnetic moment of Fe atom.

|                           | experiments         | PBE   | PBE+U |
|---------------------------|---------------------|-------|-------|
| $a_0=b_0=c_0$ (Å)         | 5.63 <sup>41</sup>  | 5.67  | 5.70  |
| $\alpha = \beta = \gamma$ | 59.35 <sup>41</sup> | 59.22 | 59.11 |

|                        |                    |      |      |
|------------------------|--------------------|------|------|
| $E_g$ (eV)             | 2.50 <sup>43</sup> | 1.04 | 2.44 |
| $\mu_{Fe}$ ( $\mu_b$ ) | 3.75 <sup>42</sup> | 3.62 | 4.11 |

In order to gain a clearer insight into the conduction properties of Ni-, Cu-, and Ag-doped BFO, we first calculated the defect formation energies  $\Delta H_f(\alpha_\beta, 0)$  of the three metals in BFO using SPBE as shown in Table 3, where  $\alpha$  is Ni, Cu, and Ag,  $\beta$  is Fe and Bi. From Table 3, it can be observed that the formation energies of all dopants under the oxygen-rich conditions are lower than those under the oxygen-poor conditions, indicating that the doping processes can be realized under the oxygen-rich conditions. The calculated results show that the dopants Ni and Cu prefer to occupy the Fe sites, while the dopant Ag is inclined to substitute the Bi site. It is noticed that the defect formation energies of  $Ni_{Fe}$  and  $Ag_{Bi}$  are negative under the oxygen-rich conditions, which means that they can be doped in BFO without external energy consumption, providing high concentration doping avenue for BFO.

Table 3. The calculated defect formation energy  $\Delta H_f(\alpha_\beta, 0)$  of various defects calculated by spin-polarized PBE (SPBE) under the oxygen-rich and oxygen-poor conditions. The  $\alpha$  is the doped atom. The  $\mu_O$  and  $\mu_\alpha$  are the chemical potential of oxygen and doped atoms.

| $\alpha_\beta$ | $\Delta H_f(\alpha_\beta, 0)$ (eV) |                       |
|----------------|------------------------------------|-----------------------|
|                | $\mu_O = 0.0$ eV                   | $\mu_\alpha = 0.0$ eV |
|                | (oxygen-rich)                      | (oxygen-poor)         |
| $Ni_{Fe}$      | -0.22                              | 1.69                  |
| $Cu_{Fe}$      | 0.07                               | 2.07                  |
| $Ni_{Bi}$      | 0.66                               | 2.54                  |
| $Cu_{Bi}$      | 0.81                               | 2.78                  |
| $Ag_{Fe}$      | 0.37                               | 3.31                  |
| $Ag_{Bi}$      | -0.16                              | 2.75                  |

The defect formation energies  $\Delta H_f(\alpha_\beta, 0)$  as a function of Fermi energy level for  $Ni_{Fe}$ ,  $Cu_{Fe}$ , and  $Ag_{Bi}$  are shown in Fig. 2. The transition energy levels of the defects are represented by the solid dots, which are reference to the VBM of pristine BFO. Our electronic structure calculations have revealed that all three dopants are acceptors making BFO *p*-type semiconductor.  $Ni^{2+}$  and  $Cu^{2+}$  ion occupying the  $Fe^{3+}$  site creates a single acceptor state, while  $Ag^+$  ion occupying a Bi site creates double acceptor states above the VBM of pristine BFO. The calculated transition energy level  $\epsilon_{Ni_{Fe}}(0/-)$  is of 0.26 eV,  $\epsilon_{Cu_{Fe}}(0/-)$  is of 0.60 eV,  $\epsilon_{Ag_{Bi}}(0/-)$  is of 0.39 eV, and  $\epsilon_{Ag_{Bi}}(0/2-)$  is of 0.44 eV. These results indicate that the acceptor level created by  $Ni_{Fe}$  is shallower than that created by  $Cu_{Fe}$ ,

suggesting that  $\text{Ni}_{\text{Fe}}$  can be readily ionized, giving rise to high conductivity. Meanwhile  $\text{Ag}_{\text{Bi}}$  also enhance the conductivity of BFO by introducing two acceptor levels, in other words, by increasing the concentration of holes.

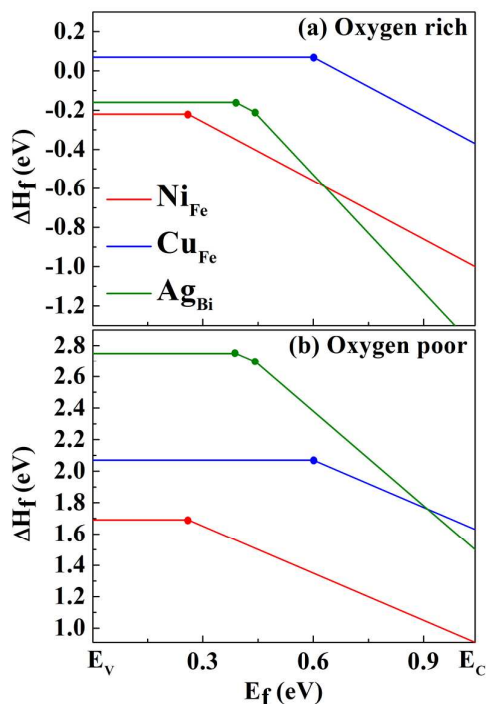


Fig. 2 (Color Online) The defect formation energy of BFO doped with Ni, Cu and Ag atom as a function of the Fermi energy in the band gap of BFO for oxygen-rich and oxygen-poor conditions. The solid lines represent charge states of the defect. The solid dots represent the transition energy levels  $\epsilon_\alpha(0/q)$  of defects.  $E_v$  and  $E_c$  denote positions of the valence band maximum (VBM) and the conduction band minimum (CBM) of the host, respectively. Only the most stable charge state of a defect is shown.

The defect formation energies  $\Delta H_f(\text{Ni}_{\text{Fe}}, 0)$  is lower than  $\Delta H_f(\text{Cu}_{\text{Fe}}, 0)$ , and the transition energy level  $\epsilon_{\text{Ni}_{\text{Fe}}}(0/-)$  is also shallower than  $\epsilon_{\text{Cu}_{\text{Fe}}}(0/-)$  as shown in Fig 2. The reason can be understood in the following manner: The induced acceptor level from substitutional dopants at Fe sites is derived mostly from the VBM state of pristine BFO, which is mainly dominated by  $\text{O}_{2p}$  state mixed with  $\text{Fe}_{3d}$  state, shown in Fig. 1(b). Because both the  $p$  and  $d$  orbitals have the same  $t_{2g}$  symmetry in the octahedral structures, there is strong  $p$ - $d$  coupling between the two states<sup>45</sup>, pushing the acceptor levels higher in energy. For the Ni and Cu, the orbital energy of  $\text{Ni}_{3d}$  is lower in energy than that of  $\text{Cu}_{3d}$ , thus the  $p$ - $d$  coupling of  $\text{Cu}_{3d}$  and  $\text{O}_{2p}$  is stronger, making its acceptor level deeper than that of  $\text{Ni}_{3d}$ .<sup>46</sup> In Fig. 3, we show the

pDOS of doped BFO calculated using SPBE+U. In panels (a) and (b), we find that the defect level introduced by Ni<sub>Fe</sub> is mainly comprised of O<sub>2p</sub> state mixed with Ni<sub>3d</sub> and Fe<sub>3d</sub> states. In panels (c) and (d), the components of Cu<sub>Fe</sub> defect level are similar to those of Ni<sub>Fe</sub>, for example, O<sub>2p</sub> state mixes to small degree with Cu<sub>3d</sub> and Fe<sub>3d</sub> states. In addition, the ion size of Fe<sup>3+</sup> is 0.69 Å, smaller than Ni<sup>2+</sup> (0.83 Å) and Cu<sup>2+</sup> (0.87 Å). The larger ion size of defect generates larger compress strain on the oxygen atoms surrounding the defect. Thus, the higher  $\Delta H_f(\text{Cu}_{\text{Fe}}, 0)$  is caused by the large *p-d* coupling of Cu<sub>3d</sub> and O<sub>2p</sub> and the defect strain effect induced by the larger radius of Cu<sup>2+</sup>. In the case of dopant Ag, Ag<sup>+</sup> has a much larger size (1.29 Å) than Fe<sup>3+</sup>, thus its larger strain effect make its defect formation energy  $\Delta H_f(\text{Ag}_{\text{Fe}}, 0)$  higher than  $\Delta H_f(\text{Ag}_{\text{Bi}}, 0)$ . In Fig. 3(e) and 3(f), the defect level is only comprised of O<sub>2p</sub> and Fe<sub>3d</sub> states because the 4d orbitals of Ag<sup>+</sup> are fully occupied. The transition energy level  $\varepsilon_{\text{Ag}_{\text{Bi}}}(0/-)$  is higher than  $\varepsilon_{\text{Ni}_{\text{Fe}}}(0/-)$  and lower than  $\varepsilon_{\text{Cu}_{\text{Fe}}}(0/-)$ , because the orbital energy of Ag<sub>4d</sub> is lower than that of Cu<sub>3d</sub> and higher than that of Ni<sub>3d</sub>, resulting in a stronger O<sub>2p</sub> and Ag<sub>4d</sub> *p-d* coupling than that of O<sub>2p</sub> and Ni<sub>3d</sub>, but a weaker *p-d* coupling than that of O<sub>2p</sub> and Cu<sub>3d</sub>.

To validate the theoretical calculations we performed a series of doping experiments of Ni<sup>2+</sup>, Ag<sup>+</sup> and Cu<sup>2+</sup> in BFO nanofibers. Fig. 4 (a)-(d) shows the surface morphologies of the pristine and doped BFO nanofibers taken by field emission scanning electron microscope. It is observed that the morphology of the nanofibers changed with the addition of dopants. The nanofibers doped with Ni displayed smooth surface morphology as compared to Cu and Ag doping. The diameters of the calcined nanofibers were in the range of 20-130 nm. Some nanofibers with larger diameter of ~ 150 nm were observed for the Ag doping case. The size distribution histogram of the pristine and doped nanofibers is shown below the respective SEM images. The average diameters of the nanofibers were 61 nm, 48 nm, 73 nm and 69 nm corresponding to pristine, Ni doped, Ag doped and Cu doped samples respectively.

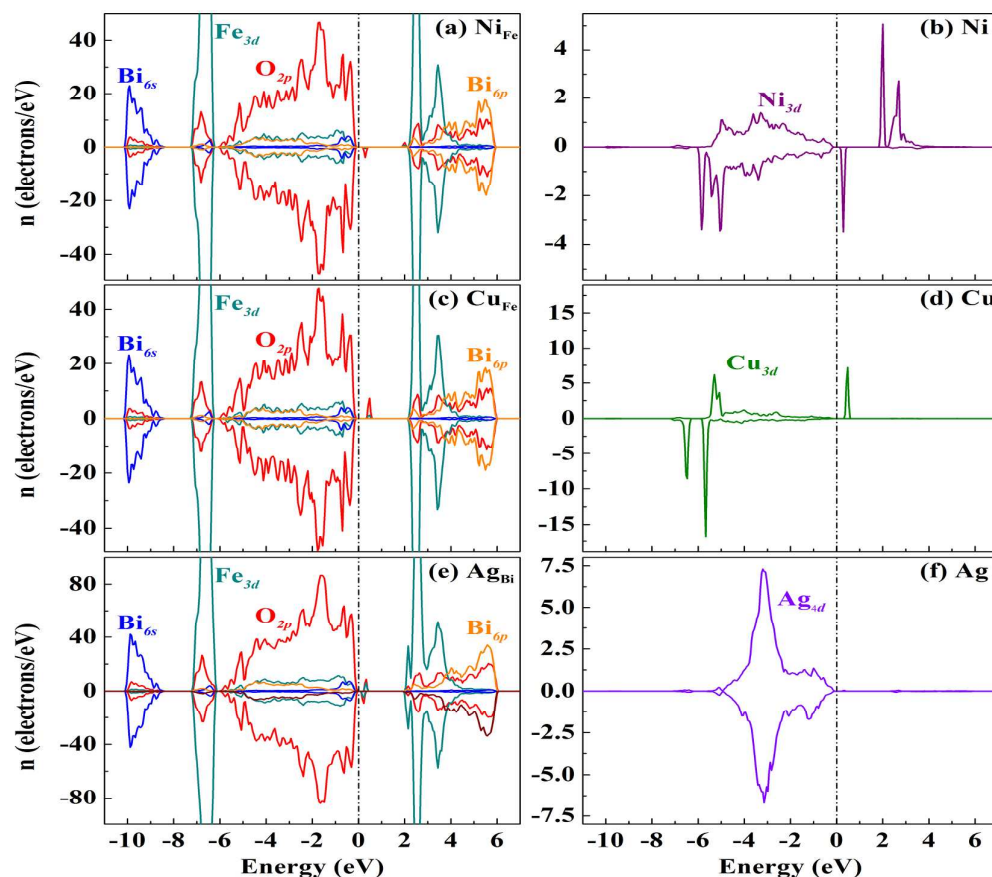


Fig. 3 (Color Online) The projected density of states of BFO doped with Ni, Cu, and Ag, respectively. The dash-dot vertical line is at the Fermi level of BFO referenced to valence band maximum (VBM) of host.

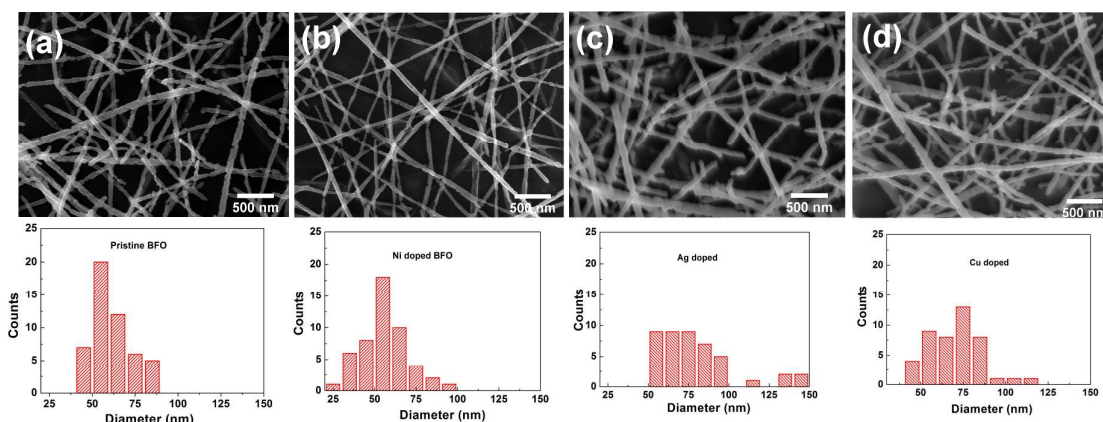


Fig 4: FE-SEM images of BFO nanofibers synthesized by electrospinning method and corresponding size distribution histograms of (a) Pristine (b) Ni-doped (c) Ag-doped and (d) Cu-doped.

The phases of the nanofibers were investigated by XRD as shown in Fig 5 (a). It is observed that all the samples exhibit single phase perovskite structure with a small amount of

non-perovskite phase such as  $\text{Bi}_2\text{Fe}_4\text{O}_9$  present. Comparison of the experimental data with the standard Powder Diffraction File (PDF) indicates that all the expected peaks originating from  $\text{BiFeO}_3$  structure are present.<sup>47</sup> All the four samples are indexed as rhombohedral structure with R3c space group. Structural phase transition is not observed in the samples. When Ni ions are doped in BFO, the doublet peaks around  $32^\circ$  slightly shift toward lower angle direction, presumably because the radius of  $\text{Ni}^{2+}$  (0.075 nm) is larger than that of the  $\text{Fe}^{3+}$  (0.069 nm). For  $\text{Ag}^+$  and  $\text{Cu}^{2+}$  doping, Ag will substitute Bi atoms and Cu substitutes Fe atoms as predicted by DFT calculations above, and similarly, the doublet peak shifts towards lower angle as both  $\text{Ag}^+$  and  $\text{Cu}^{2+}$  are larger than Bi and Fe respectively. The crystalline structure of BFO nanofibers is further examined by HRTEM, as shown in Fig. 5(b). The selected area electron diffraction (SAED) pattern in the inset of Fig. 5(b) shows very sharp diffraction spots, proving the well-developed single-crystalline structure. The regular spacing of the observed lattice are 0.396 and 0.278 nm, which corresponds to the (012) and (110) crystal planes of a rhombohedral BFO phase, respectively.

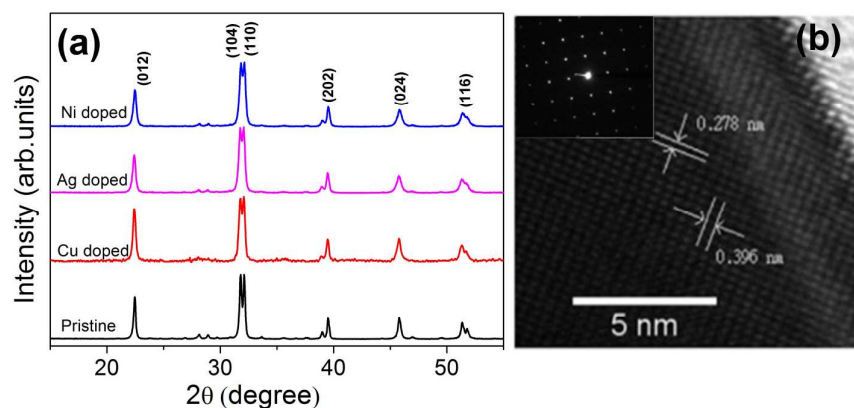


Fig 5: (a) XRD diffraction pattern of pristine and doped BFO nanofibers. (b) HRTEM image of pristine BFO nanofibers. Inset shows the selected area diffraction pattern (SAED).

We now investigate the electrical conduction of the pristine and doped BFO nanofibers. Fig 6 shows the plots of the current density ( $\text{A}/\text{cm}^2$ ) as a function of applied voltage (V). The current increases when BFO is doped with Ni, Ag and Cu. It is observed that Ni doping increases the current, followed by Ag and Cu. The value of current density for Ni, Ag and Cu doping at 5 V were  $3.68 \times 10^{-4} \text{ A}\cdot\text{cm}^{-2}$ ,  $2.67 \times 10^{-4} \text{ A}\cdot\text{cm}^{-2}$ , and  $1.02 \times 10^{-4} \text{ A}\cdot\text{cm}^{-2}$ , respectively. These experimental results can be explained from our DFT calculations as shown in Fig 2, which show that the transition energy level for  $\text{Ni}_{\text{Fe}}$  is 0.26 eV, 0.60 eV for

$\text{Cu}_{\text{Fe}}$ , and 0.30 and 0.44 eV for  $\text{Ag}_{\text{Bi}}$ . In other words, the acceptor level created by  $\text{Ni}_{\text{Fe}}$  is shallower than that created by  $\text{Cu}_{\text{Fe}}$  suggesting that it can be readily ionized to grant higher conductivity as displayed in Fig 6.  $\text{Ag}_{\text{Bi}}$  also enhances the conductivity of BFO by introducing two acceptor levels, but the conduction is still lower than  $\text{Ni}_{\text{Fe}}$  because the acceptor levels are deeper than that of  $\text{Ni}_{\text{Fe}}$ .

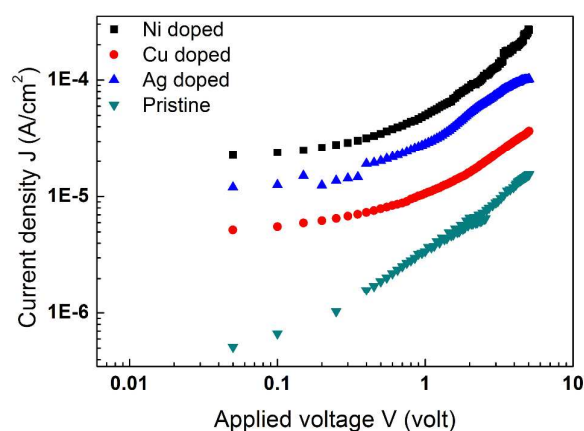


Fig 6: Representative curves of current density versus applied voltage of pristine and Ni-, Cu-, and Ag-doped BFO nanofibers.

## Conclusion

Our study shows that doping BFO with Ni approaches the conductivity limit. This was accomplished by first screening all transition metals with a semi-empirical approach (e.g., radius size, and Gibb's free energy of ionization). This approach was followed by further analysis using first-principles calculations, which were then corroborated through experiment. Application of the above-mentioned method shows that  $V_{\text{Bi}}$  are the dominant factor determining the conductivity in BFO at oxygen-rich conditions, which implies that controlling the concentration of holes by *p*-type doping can effectively tune the conductivity of BFO. The calculated results show that Ni and Cu atoms prefer to substitute Fe sites to form acceptors, however, Ag atoms favor the substitution of Bi sites to form double acceptors. As a result, all three dopants increase the overall concentration of holes in BFO. Beyond theoretical predictions, our experimental results also confirm that the conductivities of Ni-, Cu- and Ag-doped BFO nanofibers significantly increase. Similar studies based on the methodology presented here may be conducted to search for the limiting conductivity in other photocatalytic systems, such as ZnO, TiO<sub>2</sub>, SnO<sub>2</sub> and PbTiO<sub>3</sub>.<sup>18-21</sup>

## Acknowledgements

Funding for this project was provided by SUTD-ZJU (ZJURP1200101) and MOE Tier2 (T2 MOE1201-Singapore) grants.

## Notes and references

<sup>a</sup>*Entropic Interface Group, Engineering Product Development, Singapore University of Technology and Design, 20 Dover Drive, Singapore 138682.*

<sup>b</sup>*School of Materials Science & Engineering, Nanyang Technological University (NTU), 50 Nanyang Avenue, Singapore 639798.*

E-mail: wuping@sutd.edu.sg

1. Y. N. Venetsev, G. Zhadanov and S. Solov'ev, *Sov. Phys. Crystallogr.*, 1960, **4**, 538.
2. S. V. Kiselev, P. R. Ozerov and G. S. Zhdanov, *Sov. Phys. DOKLADY*, 1963, **7**, 742.
3. V. G. Bhide and M. S. Multani, *Solid State Commun.*, 1965, **3**, 271.
4. J. M. Moreau, C. Michel, R. Gerson and W. J. James, *J. Phys. Chem. Solids*, 1971, **32**, 1315.
5. J. Wang, J. B. Neaton, H. Zheng, V. Nagarajan, S. B. Ogale, B. Liu, D. Viehland, V. Vaithyanathan, D. G. Schlom, U. V. Waghmare, N. A. Spaldin, K. M. Rabe, M. Wuttig and R. Ramesh, *Science*, 2003, **299**, 1719.
6. C. Ederer and N. A. Spaldin, *Phys. Rev. Lett.*, 2005, **95**, 257601.
7. J. B. Neaton, C. Ederer, U. V. Waghmare, N. A. Spaldin and K. M. Rabe, *Phys. Rev. B*, 2005, **71**, 014113.
8. H. Naganuma and S. Okamura, *J. Appl. Phys.*, 2007, **101**, 09M103.
9. G. W. Pabst, L. W. Martin, Y. H. Chu and R. Ramesh, *Appl. Phys. Lett.*, 2007, **90**, 072902.
10. X. Qi, J. Dho, R. Tomov, M. G. Blamire and J. L. MacManus-Driscoll, *Appl. Phys. Lett.*, 2005, **86**, 062903.
11. H. Uchida, R. Ueno, H. Funakubo and S. Kodo, *J. Appl. Phys.*, 2006, **100**, 014106.
12. K. Brinkman, T. Iijima and H. Takamura, *Jap. J. Appl. Phys.*, 2007, **46**, L93.
13. P. Kharel, S. Talebi, B. Ramachandran, A. Dixit, V. M. Naik, M. B. Sahana, C. Sudakar, R. Naik, M. S. R. Rao and G. Lawes, *J. Phys.: Condens. Matter*, 2009, **21**, 036001.
14. K. Abe, N. Sakai, J. Takahashi, H. Itoh, N. Adachi and T. Ota, *Jap. J. Appl. Phys.*, 2010, **49**, 09MB01.
15. J. G. Wu and J. Wang, *Solid-State Lett.*, 2010, **13**, G83.
16. Z. Zhang, P. Wu, L. Chen and L. Wang, *Appl. Phys. Lett.*, 2010, **96**, 012905.
17. Q. Xu, M. Sobhan, Q. Yang, F. Anariba, K. P. Ong, and P. Wu, *Dalton Tans.*, 2014, **43**, 10787.
18. Z. G. Yu, H. Gong, and P. Wu, *Chem. Mater.*, 2005, **22**, 852.
19. C. S. Chou, Y. H. Huang, P. Wu, and Y. T. Kuo, *Appl. Energ.*, 2014, **118**, 12.
20. A. Katoch, G. J. Sun, S. W. Choi, S. Hishita, V. V. Kulish, P. Wu, and S. S. Kim, *Sci. Rep.*, 2014, **4**, 4622.
21. Z. Zhang, P. Wu, L. Li, and C. Shu, *Appl. Phys. Lett.*, 2006, **88**, 142902.
22. L. Q. Jian, J. K. Kuo, H. B. Liu, M. Zhu, X. Zhou, P. Wu, and C. H. Li, *J. Phys. Chem. Solid*, 2006, **67**, 1531.
23. C. Li, K. C. K. Soh, P. Wu, *J. Alloy. Compd.*, 2004, **372**, 40.
24. P. Wu and C. H. Li, *Calphad*, 2003, **27**, 201.
25. C. H. Li and P. Wu, *Chem. Mater.*, 2001, **13**, 4642.
26. Y. Zeng, P. Mao, S. P. Jiang, P. Wu, L. Zhang, and P. Wu, *J. Power Sour.*, 2011, **196**, 4524.
27. [http://www.webelements.com/atom\\_sizes.html](http://www.webelements.com/atom_sizes.html).
28. H. Naganuma, Chapter 16 Multifunctional Characteristics of B-site Substituted BiFeO<sub>3</sub> Films, edited by M. Lallart, *Ferroelectrics-Physical Effects*, published by InTech, 2011.
29. P. E. Blöchl, *Phys. Rev. B*, 1994, **50**, 17953.
30. J. P. Perdew, K. Burke and M. Ernzerhof, *Phys. Rev. Lett.*, 1996, **77**, 3865.
31. G. Kresse and J. Furthmüller, *Phys. Rev. B*, 1996, **54**, 11169.
32. H. J. Monkhorst and J. D. Pack, *Phys. Rev. B*, 1976, **13**, 5188.
33. S. L. Dudarev, G. A. Botton, S. Y. Savrasov, C. J. Humphreys, and A. P. Sutton, *Phys. Rev. B*, 1998, **57**, 1505.
34. T. Higuchi, Y. -S. Liu, P. Yao, P. -A. Glans, J. Guo, C. Chang, Z. Wu, W. Sakamoto, N. Itoh, T. Shimura, T. Yogo, and T. Hattori, *Phys. Rev. B*, 2008, **78**, 085106.

35. J. A. McLeod, Z. V. Pchelkina, L. D. Finkelstein, E. Z. Kurmaev, R. G. Wilks, A. Moewes, I. V. Solovyev, A. A. Belik, and E. T. Muromachi, *Phys. Rev. B*, 2010, **81**, 144103.
36. F. Cincini, L. Giordano, and G. Pacchioni, *Phys. Rev. B*, 2006, **74**, 165403.
37. M. Heinemann, B. Eifert, and C. Heiliger, *Phys. Rev. B*, 2013, **87**, 115111.
38. N. Umezawa, O. Shuxin, J. Ye, *Phys. Rev. B*, 2011, **83**, 035202.
39. S. B. Zhang and J. E. Northrup, *Phys. Rev. Lett.*, 1991, **67**, 2339.
40. S. -H. Wei, *Comput. Matter.Sci.*, 2004, **30**, 337.
41. F. Kubel and H. Schmid, *ActaCrystallogr., Sect. B: Struct. Sci.*, 1990, **46**, 698.
42. I. Sosnowska, W. Schäfer, W. Kockelmann, K. H. Andersen and I. O. Troyanchuk, *Appl. Phys. A: Mater. Sci. Process.*, 2002, **74**, S1040.
43. F. Gao, Y. Yuan, X. Y. Chen, F. Chen, J. M. Liu and F. Z. Ren, *Appl. Phys. Lett.*, 2006, **89**, 102506.
44. A. Walsh, G. W. Watson, D. J. Payne, R. G. Edgell, J. H. Guo, P. A. Glans, T. Learmonth, and K. E. Smith, *Phys. Rev. B*, 2006, **73**, 235104.
45. T. Wolfram and S. Ellfältioğlu, *Electronic and Optical Properties of d-band Perovskites*, Cambridge University Press, 2006.
46. Y. Yan and S. -H. Wei, *Phys. Stat. Sol. (b)*, 2008, **245**, 641.
47. M. Sobhan, Q. Xu, Q. Yang, F. Anariba, and P. Wu, *Appl. Phys. Lett.*, 2014, **104**, 051606.